# UC Davis
## UC Davis Previously Published Works

**Title**

Two-Color Volumetric Imaging of Neuronal Activity of Cortical Columns

**Permalink**

**Journal**

**ISSN**

**Authors**

Han, Shuting
Yang, Weijian
Yuste, Rafael

**Publication Date**

**DOI**

# Two-Color Volumetric Imaging of Neuronal Activity of Cortical Columns

**Shuting Han**[1,3,4,*], **Weijian Yang**[1,2,3], and **Rafael Yuste**[1]

[1]Neurotechnology Center, Department of Biological Sciences, Columbia University, New York, NY 10027, USA

[2]Present address: Department of Electrical and Computer Engineering, University of California, Davis, Davis, CA 95616, USA

[3]These authors contributed equally

[4]Lead Contact

## SUMMARY

To capture the emergent properties of neural circuits, high-speed volumetric imaging of neural activity at cellular resolution is needed. Here, we introduce wavelength multiplexing to perform fast volumetric two-photon imaging of cortical columns (>2,000 neurons in 10 planes at 10 vol/s), using two different calcium indicators, an electrically tunable lens and a spatial light modulator. We image the activity of neuronal populations from layers 2/3 to 5 of primary visual cortex from awake mice, finding a lack of columnar structures in orientation responses and revealing correlations between layers which differ from trial to trial. We also simultaneously image functional correlations between presynaptic layer 1 axons and postsynaptic layer 2/3 neurons. Wavelength multiplexing enhances high-speed volumetric microscopy and can be combined with other optical multiplexing methods to easily boost imaging throughput.

## Graphical Abstratct

## In Brief

In this work, Han et al. demonstrate two-color two-photon volumetric imaging of cortical neurons from layer 2–5 *in vivo* from more than 2,000 neurons at 10 vol/s. This scheme is compatible with many other imaging techniques, providing a new tool for high-throughput volumetric imaging.

## INTRODUCTION

High-speed volumetric imaging of neural activity at cellular resolution is an important method to decipher the function of microcircuits at a population level. Because the mammalian cortex is organized into layers, the coordinated activity of neurons within and across layers likely contributes to the emergent functional properties of circuit, making it necessary to measure neuronal activity in three dimensions (Alivisatos et al., 2012). Calcium imaging provides a powerful tool for recording the activity from a large population of neuron *in vivo* (Tian et al., 2009; Yuste and Katz, 1991). In combination with two-photon imaging, it allows the observation of neuronal activity deep in brain tissue (Denk et al., 1990; Helmchen and Denk, 2005; Yuste and Denk, 1995). However, conventional two-photon calcium imaging is constrained to imaging a single two-dimensional (2D) plane. To extend it to a three-dimensional (3D) volumes, while maintaining cellular resolution and high temporal resolution, multiple strategies have been developed (Ji et al., 2016; Yang and Yuste, 2017). Focusing devices such as piezo-controlled objectives (Peron et al., 2015; Göbel and Helmchen, 2007), spatial light modulators (SLMs) (Yang et al., 2016),

electrically tunable lenses (ETLs) (Grewe et al., 2011), and remote focusing units (Botcherby et al., 2008; Rupprecht et al., 2016) are capable of switching focus at various speeds over a relatively large depth range (up to ~500 μm) and have been demonstrated for volumetric imaging. Although piezo-controlled objectives may perturb the sample mechanically and require longer settling time, ETLs, SLMs, and remote focusing units are decoupled from the sample and can operate on faster scale, enabling high-speed sequential scanning in depth (z). In addition, optical multiplexing strategies have been applied to increase the throughput of two-photon imaging, such as holographic imaging with SLMs, in which multiple beamlets are generated to simultaneously image multiple planes across >500 μm, with their signals demixed using statistical algorithms (Pnevmatikakis et al., 2016; Yang et al., 2016

Here we use wavelength multiplexing and combine it with fast z-scan devices as a hybrid approach for fast volumetric imaging. We labeled superficial and deep neuronal populations with calcium indicators of two different colors and simultaneously excited each neuronal population with a laser of a different wavelength. To minimize scattering, we chose GCaMP6 (Chen et al., 2013) for superficial layers (layers 2/3), and the red-shifted jRGE-CO1b (Dana et al., 2016) for deep layers (layer 5). We used an ETL for fast sequential z scanning in superficial layers and an SLM for deep layers through wavefront shaping, simultaneously. We demonstrate imaging 10 planes over 450 μm spanning from layer 2 to layer 5 in primary visual cortex (V1) of awake mice at 10 vol/s, reconstructing the activity of more than 2,000 neurons at this sampling rate. We further show simultaneous volumetric imaging of layer 1 local dendrites with layer 2/3 somata, and long-range projections from prefrontal cortex (PFC) in layer 1 of V1 with local layer 2/3 population. We identify visually evoked neuronal ensembles in three dimensions, finding a lack of columnar structures in visually evoked responses and correlations between cortical layers that vary from trial to trial and cannot be captured in sequential imaging. The wavelength multiplexing approach can be easily combined with many currently available methods, greatly enhancing fast high-throughput volumetric imaging.

## RESULTS

### Two-Color Two-Photon Microscope

Our microscope consists of two beam paths with two separate two-photon lasers, exciting green and red calcium indicators. The beam path for green indicator (GCaMP6) includes an ultrafast laser (920 nm), a telescope that expands the beam to fill the ETL, and an ETL for fast sequential defocusing. The beam path for red indicator (jRGECO), based on a previous design (Yang et al., 2016), has an ultrafast laser (1,064 nm), a telescope for beam expansion, and an SLM for generating holographic focal planes. A negative offset lens conjugate with the imaging plane was used to shift the SLM path 200 μm deeper than the ETL path (Figure 1A). Placing the 1,064 nm laser with red indicator in the deep layers benefits from less scattering of longer wavelength excitation and emission. The two lasers combine at a dichroic mirror and are then scanned by a resonant scanner and a galvanometric scanner, simultaneously exciting the sample at different depths. The emitted fluorescence is separated by another dichroic mirror and collected by two photomultiplier tubes (PMTs) with filters

optimized for corresponding fluorophores. Additionally, in order to optimize for large-angle scanning, we adopted the relay lens complex design between the two scanners on the basis of a previous study (Stirman et al., 2016) (Figure 1B). For volumetric imaging *in vivo,* two planes of ~200 μm apart are excited and recorded simultaneously; the dual focal planes are directed to a set of depths that covers two separate volumes in synchronous through ETL and SLM (Figure 1C).

To optimize for deep-layer imaging and to compensate for the optical aberrations in the system, we also implemented adaptive optics (AO) with the SLM in the 1,064 nm excitation path. We modeled the wavefront aberrations with a combination of Zernike polynomial aberration modes, measured their coefficients using fluorescent beads (Love, 1997), then corrected for the wavefront using the SLM (Figure S1; STAR Methods). AO improves both the target intensity and the point-spread function (PSF) over a defocus range of ±200 μm, reaching a minimum full width at half maximum (FWHM) of 6 μm at +150 mm defocus with a maximum of 12 μm at −200 μm defocus (Figures S2B and S2D). Wavefront correction for the ETL path is less critical, as it images superficial layers; the minimum FWHM is 8 μm at 0 μm defocus and the maximum 16 μm at −200 μm defocus (Figures S2A and S2C).

To ensure that the signals we recorded from the simultaneous dual planes do not interfere, we characterized the cross-channel contamination of our system. We imaged mice V1 *in vivo* by turning on the 920 nm laser only, or the 1,064 nm laser only, while recording signals from both PMTs simultaneously (Figure S3B). In this case, signals from the non-exciting channel represent potential contamination. We then analyzed the signal and noise from both channels with single laser excitation. For both single laser excitations, the desired signal (green for 920 nm excitation in Figure 1D, red for 1,064 nm excitation in Figure 1H) are much higher than the cross-channel contamination (red in Figure 1D, green in Figure 1H), while the noise exhibits similar patterns (Figures 1E and 1I). Overall, the signal-to-noise ratio (SNR) is much higher in the desired channel (Figures 1F and 1J). Under the situation in which both lasers are exciting, there are two types of noise in our system for each imaging channel: (1) noise from single laser excitation (represented by noise in Figure 1E for Ch1) and (2) noise from crosstalk of the other laser (represented by signal in Figure 1H and noise in Figure 1I for Ch1). The effective noise of each channel is obtained by adding up these two types of noise. Our calculation shows that the signal is substantially higher than the effective noise in both channels (Figures 1G and 1K). We conclude that our system has minimal cross-channel contamination and is optimized for simultaneous two-color imaging.

### *In Vivo* Volumetric Imaging of Cortical Columns

We applied our system to image the cortical activity of neurons from awake mice V1. We labeled the V1 neuron population with the green GCaMP6s (Chen et al., 2013) and the red jRGECO1b (Dana et al., 2016) through viral vectors. We used the ETL beam path to image GCaMP6s with 5 planes spanning from 150 to 350 μm in upper layers and the SLM beam path to image jRGECO1b with 5 planes spanning from 400 to 600 μm in deeper layers, all spaced with intervals of 50 μm (Figure 2A; Video S1). This wavelength multiplexing strategy with two beam paths together achieved a total of 10 imaging planes across 450 μm

depth with a field of view (FOV) of ~500 × 500 μm at each plane, covering from the top of layer 2 through layer 5 at 10.4 vol/s. In the example shown in Figure 2A, we recorded the spontaneous activity over a 10 min period from a total population of 1,497 cells. In our best dataset, we achieved 2,084 cells in a 500 × 500 μm FOV from 150 to 600 μm cortical depth,at 10.4 vol/s (Figure S4).

We then extracted the fluorescence traces from every neuron by a modified version of a constrained nonnegative matrix factorization (CNMF) algorithm (Pnevmatikakis et al., 2016). This version takes manual initialization of neuron locations and performs the original CNMF algorithm to automatically optimize the spatial components (shape of each potential neuron), extracts the raw fluorescence (Figures 2C and 2D, light traces; Figure S3A), filters out the noise, and calculates the deconvolved traces that represent the noiseless estimation of firing probability (Figures 2C and 2D, dark traces). Extracted traces and neuronal regions of interest (ROIs) are manually selected before further analysis on the basis of their quality. To exclude cross-channel contaminations from particularly "bright" neurons, trace pairs that are highly correlated and come from laterally overlapping ROIs in the simultaneously recorded dual planes (e.g., 150 and 400 μm planes) are kept using only the neuron with the highest SNR (STAR Methods). Figure 2A shows examples of extracted ROIs from the 10 planes after the above pre-processing steps, and Figure 2B displays their raw traces.

## Orientation Selective Cells in Cortical Columns

Although standard two-photon microscopes can image from one cortical layer at a time or a volume using z-scan devices, our microscope, through a hybrid multiplexing approach, provides a powerful tool for studying neural circuit dynamics simultaneously across layers 2–5 (L2–L5) with high spatiotemporal resolution. To demonstrate this, we recorded visually evoked activity from V1 volumes covering both L2/3 and L5 simultaneously while presenting drifting gratings of eight directions to the animals. It has been shown that subsets of mouse V1 population are tuned to orientation or direction of drifting gratings (Niell and Stryker, 2008; Rochefort et al., 2011). We indeed identified robust orientation-selective cells across the cortical column in both L2/3 and L/5 (Figures 3A-3C). For each orientation, we observed an average of 5%–8% orientation-selective cells for each of the four orientations at L2/3, in agreement with the characterization previously done using two-photon imaging (Rochefort et al., 2011), while L5 showed fewer orientation-tuned cells of 3%–7% for each of the four orientations, supporting previous results with extracellular recordings (Niell and Stryker, 2008) (Figure 3D; n = 4 mice, seven FOVs).

## Visually Evoked Neuronal Ensembles Span Superficial and Deep Layers

In neuronal circuits, individual neurons cooperate to form larger ensembles of neurons that are functionally correlated. The coactive groups, rather than single neurons, are considered to be the functional units during sensory, behavioral, and cognitive processes (Carrillo-Reid et al., 2017a; Cossart et al., 2003; Luczak et al., 2007; Mao et al., 2001; Miller et al., 2014; Yuste, 2015). One advantage of our microscope is that we can image multiple cortical layers almost simultaneously, which enables us to define and study cortical ensembles across layers on the basis of the correlation structure of the population. Several computational approaches have been proposed for ensemble detection (Avitan et al., 2017; Carrillo-Reid et al., 2015,

2017b; Lopes-dos-Santos et al., 2013); because we record from a relatively large population of neurons, we chose to use a fast graph-based community detection method (the Louvain method; Blondel et al., 2008), whose aim is to maximize modularity measurement. To detect stable ensembles, we combined the Louvain method with consensus clustering, which finds the best agreement between repetitions (Lancichinetti and Fortunato, 2012). Here we aimed to find visually evoked ensembles because of their clear functional correlation with the visual stimulus. We constructed similarity matrices from population activity during visual stimulation, detected and cross-validated neuronal ensembles with the hybrid approach of Louvain method and consensus clustering (Figure 4A; STAR Methods), and then evaluated the decoding performance of each ensemble against each visual stimulus. To do this, we generated population vectors from the ensembles, calculated the cosine similarity between the population vectors and real data, and computed the standard ROC (receiver operating characteristic) curve and AUC (area under the curve). We defined visually evoked ensembles as ensembles that are predictive of visual stimulus with an empirically defined threshold (Figure 4C). For simplicity, we combined pairs of orientations that are shown in opposite directions, resulting in ensembles for four orientations (Figures 4A-4C). The detected ensembles exhibit higher decoding performance than random sampled controls, as well as higher internal pairwise correlation (Figures 4D and 4E; n = 16 ensembles; AUC: control $0.500 \pm 0.011$ [SEM], ensemble $0.663 \pm 0.051$, $p < 0.001$; correlation: control 0.092 $\pm$ 0.017, ensemble $0.478 \pm 0.078$, $p < 0.001$, Wilcoxon signed rank test), indicating their coherent emergent activity as a group.

We then investigated the correlation structure of the ensembles between L2/3 and L5 using recorded activity during all visual stimulation trials, or using L2/3 activity during first half of all trials and L5 activity during second half of all trials. The former case represents simultaneous volumetric imaging. The latter case represents sequential imaging sessions of each layer during repetitive trials and aligning them with trial onsets, typically done with two-photon microscopes that do not have fast z-scanning devices or the z-scanning cannot cover a large span. To reduce noise in correlation structures, we investigated functional correlations only within identified visually evoked ensembles. We separated the ensemble constituent cells into L2/3 and L5 subsets and computed the pairwise correlation between these two subsets during first and second half trials or during full trials (Figure 4F). Results combined from six datasets show that correlations obtained from full trials are higher than those from half trials, and there is a lack of correlation between full trial correlation and half trial correlation (Figure 4G; $R^2 = 0.08$; half trials correlation $-0.032 \pm 0.046$, full trials correlations $0.305 \pm 0.080$, $p < 0.001$, Wilcoxon signed rank test). Background activity obtained from non-ROI pixels, however, does not differ drastically (half trials correlation $-0.005 \pm 0.010$, full trials correlation $0.084 \pm 0.014$, $p = 0.031$, Wilcoxon signed rank test). This reflects the trial-to-trial variation, possibly due to the animals' endogenous state (Carandini, 2004; Kiani et al., 2015; Kisley and Gerstein, 1999). When studying functional properties of neural circuits, it thus appears key to simultaneously capture the dynamics of the entire population of interest, because otherwise the trial-to-trial variability may dilute the correlational structure of the activity.

## Lack of Correlated Columnar Structures in Mouse V1

The visual cortex of many mammalian species is organized in a columnar spatial map in which neurons that have similar functional properties, such as orientation preference, are spatially close to each other (Bonhoeffer and Grinvald, 1991; Flubel and Wiesel, 1962). Flowever, using 2D two-photon calcium imaging, the visual cortex of rodents was originally characterized as having a salt-and-pepper structure, in which neurons with similar functional properties are intermingled (Ohki and Reid, 2007; Ohki et al., 2005). On the other hand, recent studies have reported the existence of narrow (~40–120 μm in diameter) columns of neurons with similar tuning properties in rodent V1 (Li et al., 2012; Ringach et al., 2016) and correlated columnar structures (Smith and Kohn, 2008). To investigate this, we applied our volumetric method, because we could not only analyze the orientation preference map in three dimensions (Figure 5B), but also extend the analysis to the spatial organization of cells that share emergent properties, which are identified as ensembles (Figure 5A), and functional correlation within narrow columns from the entire population. We analyzed the correlation between lateral distance (distance of xy, ignoring depth) of cell pairs and their evoked activity correlation, among all cell pairs (Figure 5C, left), among visually evoked ensembles (Figure 5C, middle), and among orientation-selective cells (Figure 5C, right). If columnar structure exists, we expect to see higher correlation in cell pairs that are distributed closer laterally. However, all of the three groups show a flat distribution, indicating uniform correlation regardless of lateral distance. We further analyzed the correlation values of cell pairs in narrow columns of 30, 50, and 100 μm during visually evoked activities. Compared with random controls in which correlation was calculated between cells within the column and a random set of cells outside of the column, none of the column diameters give significant differences (Figure 5D; n = 6 experiments; Wilcoxon rank-sum test on each correlation bin; statistics done with individual experiments). Additionally, the difference of preferred orientations among orientation-selective cells did not differ significantly with lateral distance (Figure S5). Our results thus indicate a lack of correlated columnar structure in mouse V1, extending to three dimensions the original 2D salt-and-pepper description of orientation responses (Ohki and Reid, 2007; Ohki et al., 2005), but in apparent disagreement with the reported existence of narrow vertical columns (Li et al., 2012; Ringach et al., 2016).

## Volumetric Imaging of Correlation between Long-Range Projection Axons and Local Somata

As a final demonstration of the biological utility of our method, we sought to capture the input-output correlation of a circuit, by simultaneously imaging a presynaptic axonal population and a postsynaptic population of cells. Indeed, the simultaneous two-color excitation with two lasers in our system not only expands the volume that can be imaged at once through wavelength multiplexing but also provides a tool to image and identify two distinct populations simultaneously. Using this microscope, we studied the functional correlation between the long-range axonal projections from PFC to L1 volume in V1 (labeled with GCaMP6s) and local neurons in L2/3 of V1 (labeled with jRGECO1b) (Figure 6A). We imaged the spontaneous activity of both L1 axonal projections and L2/3 somata with four planes from 25 to 100 μm in L1 and four planes from 150 to 300 μm in L2/3, achieving a volume rate of 13.0 vol/s (Figure 6B). ROIs and fluorescence traces in L2/3 were extracted using CNMF algorithm as described above, and ROIs and traces in L1 were

extracted using a recently developed simultaneous denoising, compression and demixing algorithm with penalized matrix decomposition (PMD) (Buchanan et al., 2018) (Figures 6C and 6D). The latter results in fragmented ROIs that represent putative axonal fragments and boutons with an improved SNR through denoising techniques. To group these putative ROI fragments that are potentially from the same projection, we clustered the activity traces using affinity propagation (Frey and Dueck, 2007), which does not require a cluster number input but could identify clusters of ROIs that exhibit highly correlated activity patterns (Figure 6E, four examples shown on right). Examples of these super-ROI groups are shown in Figure 6F. These ROI clusters show higher internal correlation than randomly sampled controls, indicating functional correlation (Figure 6G; n = 11 experiments; control 0.173 ± 0.005, data 0.636 ± 0.007, p < 0.001, Wilcoxon signed rank test). As the activity of long-range axonal projections and local somata are nearly simultaneously recorded, we could further use the collected dataset to investigate the correlation structure between these two populations (Figure 6H). Although the overall population correlation is distributed around zero (Figure 6J; n = 11 experiments; mean correlation 0.006 ± 0.012, p = 0.617, t test), we could identify ROI pairs from L1 PFC projection and L2/3 V1 soma that are highly correlated (Figure 6I), revealing functional relationships between these two populations.

Similarly, our system also enables volumetric imaging of L1 apical dendrites with L2/3 somata from the same population at the same time. To do so, we labeled the V1 population with a co-injection of GCaMP6s and jRGECO1b and simultaneously imaged the spontaneous activity of apical dendrites with the green path with four planes from 25 to 100 μm and somata with the red path with four planes from 150 to 300 μm, at a volume rate of 13.0 vol/s (Figures S6A and S6B). ROIs and traces were extracted as above (Figures S6C and S6D). The correlation between L1 and L2/3 is distributed slightly higher than zero (Figures S6E and S6F; n = 10 experiments; mean correlation 0.061 ± 0.011, p < 0.001, t test), confirming a stronger spontaneous functional correlation between apical dendrites and L2/3 somata, which could potentially come from the same neurons.

## DISCUSSION

### Volumetric Imaging through Wavelength Multiplexing

In this work, we extend sequential volumetric two-photon imaging with a hybrid approach that acquires two volumes simultaneously through wavelength multiplexing, combining two-color excitation and emission with ETL- and SLM-based fast z scanning. By using a red calcium indicator, jRGECO1b, that reduces the loss of photons from tissue scattering and an SLM as a z-scan device that can also implement AO to correct system aberration, we optimized our system for deep-layer imaging. We demonstrated successful volumetric calcium imaging *in vivo* of 10 planes at 10.4 vol/s, spanning across L2/3 to L5, as well as 8 planes imaging at 13.0 vol/s of L1 dendritic or axonal activity with L2/3 somatic activity. Our approach provides a method to sample a large number of neurons per second across cortical columns (>2,000 neurons sampled at 10 Hz, located over 10 planes across a depth of 450 μm, with an FOV of 500 × 500 μm per plane; see Figure S4). Further improvement can be expected with optimization of fluorophore efficiency, such as the SNR of jRGECO. Our

approach, introducing excitation wavelength multiplexing to parallelize the scanning process, provides an alternative to the volumetric imaging toolbox.

## Comparison with Other Two-Photon Volumetric Imaging Methods

Many methods have been developed for two-photon volumetric imaging (see Table S1 in Yang and Yuste, 2017, for a detailed summary). Comparing with current volumetric imaging techniques that depend on a single defocusing strategy such as piezo-controlled objectives (Göbel and Helmchen, 2007), ETLs (Grewe et al., 2011), and remote focusing (Botcherby et al., 2012), our approach is designed with two independent modules that cover two separate volumes simultaneously, thus immediately doubling the imaged volume from single volume-based systems. These two volumes are separated by their excitation and emission properties, making them optically independent of each other. The scanning speed of commonly used piezo-controlled objectives, on the other hand, is limited by the weight of objectives, especially for high-NA objectives, which tend to be heavy. In addition, comparing with acousto-optic deflectors (AODs) for random access (Duemani Reddy et al., 2008; Katona et al., 2012), which are fast but scan only selected ROIs and are therefore best for sparsely labeled samples, our method is more suitable for densely labeled samples in which more, or potentially all, pixels are of interest. Comparing with SLM-based holographic multiplexing (Yang et al., 2016), our current approach has the same advantage of simultaneously recording from two separate planes yet doubles the image volume, while keeping both volumes within the best performance range for each z-scan device (within $\pm$ 150 μm for both) and avoiding the performance decay at larger defocus planes. Additionally, through wavelength multiplexing, depth information is encoded by wavelength, and the simultaneously recorded dual planes are collected by two separate PMTs, avoiding post hoc source separation and signal demixing problems. Finally, compared with temporal multiplexing in which the laser beam is split into multiple beams with their laser pulses interleaved in time and focused at different positions (Cheng et al., 2011; Stirman et al., 2016), our approach does not require a complex data acquisition scheme and also makes full use of both lasers and is therefore more effective when imaging a large number of planes.

In terms of speed, our approach has a particularly high imaging throughput. Because the half decay time of commonly used calcium indicator (e.g., GCaMP6f) is on the order of 200–500 ms, the minimum imaging speed should be >10 Hz. With this constraint, and to the best of our knowledge, our experiment represents the most extensive imaging at this rate of a large number of neurons (2,084) over a large FOV (10 planes across 450 μm depth down to 600 μm in cortex, with an FOV of 500 × 500 μm in each plane; see Figure S4) in mice *in vivo.* Among all imaging approaches, AODs perform faster sampling of fewer pixels and are therefore ideally suited for sparse labeling. For comparison, one of the best demonstrations of AODs was an imaging of 532 cells across a 400 × 400 × 500 μm volume at 56 Hz (Katona et al., 2012). Our experiment demonstrates a 4-fold larger cell count and holds great promise for dense labeling, potentially imaging every cell in a volume. With an improved labeling efficiency, our imaging throughput could be further boosted.

Nevertheless, many of these strategies are not mutually exclusive, and wavelength multiplexing could be combined with other volumetric imaging approaches, e.g. with other

z-scan devices such as piezos, remote focusing units, or AODs, to further increase their imaging throughput. Coupled with other temporal or holographic multiplexing could further increase the speed or throughput. Our approach thus provides a general platform that can be broadly applied in combination with many currently available methods, opening more possibilities for fast high-throughput volumetric imaging.

Finally, because of the excitation spectrum overlap of GCaMP6 and RCaMP or jRGECO, a single laser, tuned between 1,020 and 1,030 nm, could be used to simultaneously image GCaMP6 and RCaMP (Inoue et al., 2015). However, because GCaMP excitation efficiency peaks at about 920–940 nm and RGECO or RCaMP between ~1,060 and ~1,150 nm (Dana et al., 2016), using a single laser to excite both indicators would compromise the fluorophore efficiency for both indicators. Our system, with two lasers set at 920 and 1,064 nm, optimizes the fluorophore performance for simultaneous two-color imaging.

## Volumetric Imaging of Large Cortical Population for Single-Trial Dynamics

The mammalian cortex is organized into six layers, and sensory information is transformed through interactions between layers (Constantinople and Bruno, 2013; Douglas and Martin, 2004). To study cortical dynamics in different layers during sensory perception or behavioral tasks, a common approach is to record from each layer of interest during repetitions of the task trials and analyze the average response, using z-scan devices such as piezo (Attinger et al., 2017; Peron et al., 2015; Kerlin et al., 2018). Although trial structures provide an important reference for the underlying cortical activity, the neural activity is intrinsically noisy and is affected by the immediate internal state of the animals (Gilbert and Sigman, 2007; Niell and Stryker, 2010), and it is still challenging to study the correlation structure between layers or areas with non-simultaneous recordings. Some commonly used methods such as piezo-controlled objectives and ETLs offer long travel range but have a trade-off between the volume or number of planes imaged, and imaging speed. Additionally, using the full range of these devices could compromise the imaging quality of longer defocus range. To study the population dynamics across multiple cortical layers, our method can simultaneously record from twice the volumes than commonly used methods, while achieving optimal imaging performance in both volumes. This provides an important tool to study cross-layer computations. As demonstrated in Figure 4, simultaneous volumetric imaging reveals a different laminar correlation structure than that could be measured using separated trials. We thus expect that our system will provide a powerful tool for studying laminar interactions in the future.

## Lack of Orientation Columns in Mouse V1

As a proof of the utility of the method to reveal spatial interaction in functional responses, we analyzed the correlational structure of the orientation responses across layers. This is a controversial issue, because the original description of unstructured orientation responses in mouse V1 ("salt and pepper" patterns of orientation) (Ohki and Reid, 2007; Ohki et al., 2005) has been questioned by reports of the existence of neurons that are arranged in narrow vertical strips and that have similar orientation responses (Li et al., 2012; Ringach et al., 2016). With our method, we could, as a third party, independently examine the validity of these claims. In our analysis, however, we find no statistically significant vertical

correlations in the orientation responses. Although we did not ascertain the clonal relation among neurons, our data are in principle inconsistent with the presence of vertical narrow "minicolumns" of orientation and suggest that orientation selectivity maps in three dimensions are disorganized in V1 of the mouse. Our method and analysis could be extended to the study of the spatial structure of other functional properties in the cortex or other neural circuits.

## Imaging the Correlation between Pre-and Postsynaptic Populations

Besides doubling the imaged volume, our two-color strategy provides a tool to image distinct neuronal population labeled with different colors at the same time. This includes examples of L1 long-range projections from other regions with local somata (Figure 6), as well as excitatory and interneuron populations (Inoue et al., 2015). Combined with its volumetric imaging ability, our system provides a tool for studying the correlation of large population of distinct subnetworks and to functionally dissect the input-output correlations of neural circuits.

In closing, we present a wavelength multiplexing design for two-photon volumetric imaging that is compatible with many other current methods. As the study of neural circuits becomes increasing more sophisticated, it is likely that there will not be a single "one shoe fits all" method to functionally dissect the interactions between many different types of neurons. Instead, we imagine a hybrid future in which different methods and probes and analysis could be flexibly combined and be properly targeted to the specific question of study. In this scenario, wavelength multiplexing should be standard, as it immediately enhances the performance of any volumetric method, increasing its range and speed.

## STAR★METHODS

Detailed methods are provided in the online version of this paper and include the following:

## CONTACT FOR REAGENT AND RESOURCE SHARING

Further information and requests for resources and reagents should be directed to and will be fulfilled by the Lead Contact, Shuting Han (shuting.han@columbia.edu).

## EXPERIMENTAL MODEL AND SUBJECT DETAILS

Experiments were performed on C57BL/6 wild-type mice, on both males and females. Experimental animals were typically postnatal (P) day P60-P120 at the time of experiments. Animals were housed on a 12h light-dark cycle with food and water *ad libitum.* All experimental procedures were carried out in accordance with the US National Institutes of Health and Columbia University Institutional Animal Care and Use Committee.

## METHOD DETAILS

**Virus injection and surgery—**Virus injection was performed between P30 and P60. For virus injection, a mixture of 200 nL AAV9.hSyn.GCaMP6s.WPRE.SV40 (UPenn Vector Core) and 700 nL AAV1.Syn.NES-jRGECO1b.WPRE.SV40 (UPenn Vector Core, 19279) was injected into both layer 2/3 and layer 5 on left V1 (from lambda: X = −2500, Y = 500, Z

= −250/−500 μm, 400/500 nL per site). Virus was injected with glass micropipets, at a rate of 80 nl/min. For experiments imaging axonal projections from PFC to L1 volume in V1, 700 nL AAV1.Syn.NES-jRGECO1b.WPRE.SV40 with 200 nL buffer (0.14M NaCl, 0.02M pH 8.0 Tris, 0.01 ‰ pluronic F68) was injected at the same location on left V1 (Z = −300 μm) between P30 and P60; two weeks after the GCaMP injection, 400 nL AAV9.hSyn.GCaMP6s.WPRE.SV40 with 200 nL buffer was injected into left PFC (from bregma: X = 300, Y = 500, Z = −900 μm). Although AAV9 has retrograde ability, we note that this is unlikely the case in our experiments, based on the following arguments: (1) in the beginning of each experiment, we adjusted the focus of both lasers path from the brain surface to ~500 μm depth, during which we observed signals in green channel with confined spatial shapes only appears within ~100 μm depth from brain surface, indicating there were no axons projecting from L5, and no GCaMP-labeled somas; (2) unpublished results from our group show that, with 400 nL injection of the same virus AAV9.h-Syn.GCaMP6s.WPRE.SV40 in the same coordinates of PFC did not show noticeable retrograde labeling of other brain areas in histology sections after ~4 weeks of expression. We therefore believe that retrograde labeling is not impacting our experiments.

Approximately 4-6 weeks after the initial injection, headplate implementation and craniotomy surgery were performed on the mice. Mice were anesthetized with isoflurane (1%–2%), injected with dexamethasone (2 mg/kg body weight, subcutaneous), enrofloxacin (4.47 mg/kg, subcutaneous), and carprofen (5 mg/kg, intraperitoneal). A custom made titanium headplate was mounted on the skull centered on V1 using dental cement. A 2 mm diameter circular cranial window was made around the injection site on left V1 with a dental drill, and the cranial window was covered by a 3 mm circular glass coverslip, sealed with cyanoacrylate adhesive. The mice were allowed to recover for at least one day before experiment, and were habituated with head-fixation prior to experiments. Mice were monitored and given analgesics (5mg/kg carprofen intraperitoneal) for two days post-procedure.

**Two-color volumetric imaging microscope**—The microscope is designed as shown in Figure 1. Two excitation lasers were used: a tunable Ti:Sapphire laser (Chameleon Ultra II, Coherent) tuned to 920 nm with a maximum output power of ~1.6W (140-fs pulse width, 80-MHz repetition rate), and an amplified fiber laser (Fianium) with a fixed wavelength at 1064 nm with a maximum output power of ~6W (200-fs pulse width, 80-MHz repetition rate). No pre-chirper was used. Each laser power is controlled with a separate Pockels cell: a Conoptics EO350-160-BK Pockels cell with a 275 driver for 920 nm laser, and a Conoptics EO350-105-BK Pockels cell with a 302 RM driver for 1064 nm laser. For 920 nm path, the beam is first expanded with a 1:7.5 telescope (focal length f1 = 40 mm, f2 = 300mm). Then, the beam passes an ETL (Optotune; EL-10-30-C-NIR-LD-MV), and is rescaled by a 4:1 telescope (f3 = 400 mm, f4 = 100 mm). For the 1064 nm path, a l/2 λ waveplate (Thorlabs; AHWP05M-980) is used to rotate the laser polarization, and the beam is expanded with a 1:4 telescope (f5 = 100 mm, f6 = 400 mm) to fill the active area of SLM. Then, the focal plane is shifted with an offset lens set [composed of two lenses (f = 500 mm, −100 mm) that contact together] with an equivalent offset of ~200 μm at imaging plane. The beam is relayed by a 1:1 telescope (f7 = 200 mm, f8 = 200mm) before being modulated by an SLM

(Meadowlark Optics; HSP512-1064; $7.68 \times 7.68$-mm$^2$ active area, $512 \times 512$ pixels). The beam is then rescaled by a 3:1 telescope (f9 = 300 mm, f10 = 100 mm). Then, both beams are combined through a dichroic mirror, scanned first by a resonant scanner (Cambridge Technology; CRS 8K resonant scanning system), then relayed by a telescope that is composed of two equivalent lens complexes (Figure 1B) (Stirman et al., 2016) installed in the opposite direction. The scan angle of the resonant scanner is $\pm 7.2°$. Since this angle is small compared to the working range of the Stirman design ($\pm14.8°$), we do not anticipate distortion at the field edges or strong field curvature. The combined beam is then scanned by a galvanometric scanner (Cambridge Technology; 6215HM40B). Both scanners are positioned at the conjugate plane to the objective pupil. The scan lens (Olympus pupil transfer lens, $f_{scan}$ = 50 mm) and tube lens ($f_{tube}$ = 180 mm) are from a modified Olympus BX-51 microscope. Imaging was done with a 25x Olympus 253 N.A. 1.05 XLPlan N objective. The imaging frame rate is 60 Hz (256×256 pixels) for single plane imaging; under this situation, we have ~254 ns/pixel, or ~20 pulses/pixel rate for both lasers. Focal planes of both paths were shifted in steps at the end of each frame; the scanner flyback time to start the next frame was set to 3 ms, during which both ETL and SLM would change the beams' focal depth.

Fluorescence emission was collected through two separate photomultiplier tubes (PMTs; Hamamatsu; H7422P-40) and two low noise amplifiers (FEMTO DHPCA-100), with a collection bandpass filter of $520 \pm 40$ nm (Chroma, ET520/40 m) for the green path, and a $630 \pm 75$ nm bandpass filter (Chroma, ET630/75 m) for the red path. The standard ScanImage 2016 (Pologruto et al., 2003) was used to control the Pockels cells, the focus of the ETL, the scanning mirrors and the digitizer for data storage, as well as image acquisition. SLM was controlled by a custom MATLAB (The Mathworks) software (Yang, 2018). Locomotion of the animals was recorded with an infared LED/photodarlington pair (Honeywell S&C HOA1877-003), which consists of a small c-shaped device positioned at the edge of the rotating wheel (striped with black tape) connected to the imaging computer as an analog input. Locomotion was detected as voltage changes in the photodarlington readout. The typical imaging power ranges between ~15 mW to ~100 mW for 920 nm laser path, and around ~200 mW for 1064 nm laser path, depending on the depth. Details of optical elements used in the system can be found in Table S1.

**Special notes in two-color volumetric imaging scheme**—The wavelength multiplexing scheme is essentially a combination of two microscopes with different two-photon excitation wavelengths. All the necessary steps used in the two-photon microscope apply here. One particularly important step for our high speed volumetric imaging is to set up the offset lens in one beam path so the focal spots of the two beam paths are separated axially. The offset lens should be placed in a conjugate plane to the back aperture of the objective lens. The collimated laser beam should be aligned to the optical axis of the offset lens to minimize aberration. The focal length of the offset lens could be calculated through thin lens equation with the consideration of the desired focus offset in the sample, and the other lens in the microscope. The two beams should be well aligned so their imaged fields of view are overlapped laterally in general, though a lateral offset could also be implemented if needed. The z-scanning device such as the ETL or SLM should be in the conjugate plane of

the back aperture of the objective, otherwise the imaged field of view could change with different focal setting on the ETL or SLM. To fully utilize the focusing effect of ETL or SLM, the beam should fill the aperture of ETL or SLM.

To achieve effective wavelength multiplexing, the two fluorophore should have a large separation in spectrum, otherwise strong cross talk could happen between the two PMT channels. In the rare case that neurons have strong emission which bleed through to another channel, steps detailed in "Image processing and signal extraction" should be implemented to remove the cross-talk.

**Adaptive optics**—As SLM is a natural choice for correcting wavefront aberration induced by both the system and samples, the excitation efficiency of the SLM path in our system can be improved by implementing adaptive optics (AO) through SLM (Love 1997; Ji et al., 2012). Here we implemented system correction by modeling wavefront aberration with the first 30 modes of Zernike polynomials. This includes common aberrations such as spherical aberration, astigmatism, coma, etc. We estimated the coefficient for each Zernike polynomial by varying the coefficient and optimizing the imaged intensity of 0.5 μm fluorescent beads. The final correcting wavefront on SLM is a combination of weighted Zernike polynomials with measured coefficients. For the best optical performance and effectiveness of AO, we optically coupled the resonance scanner and galvanometric mirror by placing them at each other's conjugate planes through the relay lens complex (Figure 1B).

**PSF measurement**—PSF was measured with 0.5 μm fluorescent beads on slides. Z stack images were taken centering on a selected bead with a range of focal depths, with an interval of 1 μm between each consecutive image. Each image were averaged from 5 imaged frames. Axial FWHM were calculated by fitting the intensity versus depth curve to a Gaussian distribution function, then taking the half width using the fitted curve. Since we aimed to achieve long defocus range with both ETL and SLM paths, we underfilled the back aperture of objective, resulting in lower effective excitation NA and thus larger PSFs. With an effective excitation NA of ~0.55, we estimate that the axial FWHM for 920 nm path would best be ~5.2 μm, and for 1064 nm path ~6 μm. The experimentally measured minimum axial FWHM for the 920 nm path was 8 μm; it is larger than 5.2 μm, mostly due to system aberration. With adaptive optics in the 1064 nm path, the minimum axial FWHM was measured to be 6 μm. Note that a higher excitation NA will make the PSF degrades faster with larger defocus, and therefore we chose a smaller excitation NA, balancing PSF size and defocus range.

**Image processing and signal extraction**—The raw imaging datasets were first motion corrected using an ImageJ plugin Moco (Dubbs et al., 2016). All imaging planes in the same datasets were registered using the same motion profile estimated from the most representative plane. Then, for somatic imaging datasets, putative neuronal regions of interest (ROIs) were initialized manually by playing through each plane of the datasets and generating a list of centroid locations using an ImageJ plugin Time Series Analyzer, in order to obtain an accurate guess of cell locations. The ROIs were then segmented by a modified version of a constrained nonnegative matrix factorization (CNMF) algorithm (Pnevmatikakis

et al., 2016) that initializes with the manual list of ROI locations, and the algorithm automatically estimates the background fluorescence, the raw fluorescence signals, the denoised (filtered) signals, and the deconvolved signals. Then, all ROIs are manually selected using a custom MATLAB GUI that displays both the shape of ROIs and the corresponding traces. ROIs that exhibit reasonable shape (having the contour that could represent a neuron), and have activity during the imaging course (not silent through the entire imaging session, with recognizable calcium events, with typical form of calcium transient) were kept. Rejected ROIs are typically due to motion artifact, or low SNR, both of which could results in variable calcium traces and contour.

We observed fewer active cells at deeper planes, which could result from light scattering effect. Since we injected jRGECO1b at 500 μm cortical depth, and that virus typically spread at least 500 μm axially in both directions after 4 weeks of expression, we believe the fewer active cells at deeper planes are not due to expression profile. Deeper planes are naturally more affected by scattering effect, especially with dense labeling in the cortex; emitted fluorescence from densely labeled tissue above naturally leads to stronger background for deeper imaged layers, making the low SNR cells lost in the noise. We believe due to such scattering effect, only high SNR cells in deeper layer were observed, resulting in a smaller number of active cells.

To remove potential duplicated cells either due to spectrum bleed through, or redundant manual seeding during ROI location initialization, we removed potentially redundant ROIs that are highly correlated, laterally close and are (a) in the same plane, or (b) from adjacent planes in the same PMT channel, or (c) from dual planes that are recorded simultaneously, from the two PMT channels (Figure S3C). ROI pairs that (1) have a Pearson correlation coefficient higher than 0.75, (2) are within 15 μm apart laterally, and satisfy one of the criteria (a-c), were regarded as redundant pairs, and only the ROI with highest signal-to-noise ratio (SNR) were kept. Approximately 10% ROIs were removed during this procedure.

For dendritic and axonal imaging datasets, a penalized matrix decomposition (PMD) algorithm was used to automatically denoise and demix the datasets, which improved the resulting SNR for noisy dendritic/axonal imaging (Buchanan et al., 2018). Then, dendritic or axonal ROIs were automatically segmented, and fluorescence traces were extracted by the algorithm. The traces were then filtered by trend filtering as described in the above reference. After that, ROIs were manually selected using the custom MATLAB GUI as described above.

**Visual Stimulation—**Visual stimuli were generated using MATLAB and the Psychophysics Toolbox (Mathworks) and displayed on a monitor (Dell; P1914Sf, 19-inch, 60-Hz refresh rate) positioned 28 cm in front of the right eye. Each animal was presented two consecutive visual stimulation sessions, each session with 15 trials, and each trial with a random order of 8 drifting gratings separated by 45°. In each trial, drifting gratings (100% contrast, 0.04 cycles per degree, 2 cycles per second) were shown for 4 s, followed by a 6 s interval with mean luminescence gray screen.

**Orientation tuning analysis—**Orientation tuning curves were calculated by averaging the ΔF/F response traces of all grating stimulus sessions. This gives the polar plots. Orientation selectivity indices were calculated using circular statistics, defined as $\text{OSI} = \left| \sum_k R_k \exp(2i\theta_k) / \sum_k R_k \right|$, where $R_k$ is the response to each orientation (k = 1-8), $i$ is the imaginary unit, and $\theta_k$ is the orientation in radians (Tzvetanov, 2016). Neurons with OSI > 0.2 were defined as orientation selective cells. The preferred orientation was determined by the orientation that evoked the strongest ΔF/F response. L2/3 was defined as 100 μm - 300 μm depth from surface, and L5 was defined as 400 μm - 600 μm from surface. We excluded L4 for analysis due to the relatively smaller number of cells recorded and reduced GCaMP labeling in some cases (Peron et al., 2015).

**Ensemble identification—**Ensembles were detected using a graph-based community detection method, the Louvain method (Blondel et al., 2008). This method aims at detecting community structures in graphs, which are subsets of highly interconnected nodes. To apply this method, we first computed the pairwise similarity matrix using the inferred (deconvolved) fluorescence traces. Running epochs were excluded in order to reduce correlation artifact. This results in a $N_{\text{neuron}}$-by-$N_{\text{neuron}}$ correlation matrix. Then, to further reduce noise, weak correlation values that are below the sum of mean and three times of standard derivation were zeroed. A MATLAB module was used to perform Louvain community detection (Rubinov and Sporns, 2010). This method does not require a cluster number input, however, a resolution parameter $\gamma$ was used to control the size of output communities, with $\gamma = 1$ resulting in classic communities, $\gamma < 1$ detecting larger communities, and $\gamma > 1$ detecting smaller communities. We ranged $\gamma$ between 1 and 1.5 with an interval of 0.05, performed community detection with each $\gamma$ and cross-validated using the visual stimulus prediction performance of the resulting communities, taking the $\gamma$ that gives best overall prediction performance. To calculate visual stimulus prediction performance, we considered the detected communities as $N_{\text{neuron}}$-by-1 population vectors, where entries corresponding to the constituent neurons in the communities are 1, and others are 0. We computed the cosine similarity between these community population vectors and real data, and used the output similarity values to compute the standard receiver operating characteristic (ROC) curves and the area under curve (AUC). AUC = 0.5 represents chance level, while larger than 0.5 represents positive predictions, and smaller than 0.5 represents negative predictions. For each detected community, we summed the AUC values for each grating direction, and combined the opposite directions to be a single orientation. For each orientation, communities that have an average AUC higher than 10% above chance level (0.55) were considered to be visually-evoked ensembles.

**Clustering of axonal activity—**We used affinity propagation to cluster axonal activity in layer 1 (Frey & Dueck 2007). This method operates on the pairwise similarity matrix between all pairs of data points, and identify the exemplers based on an input preference vector, then automatically determines the number of clusters. The preference vector was set to 95% quantile of the similarity matrix here. The MATLAB module used is available at [https://www.psi.toronto.edu/index.php?q=affinity%20propagation] (without sparsity).

## QUANTIFICATION AND STATISTICAL ANALYSIS

Details of statistical analysis method, sample size, type of sample and significance level can be found in corresponding figure legends. Statistics was done by Wilcoxon rank-sum test for unpaired samples, and Wilcoxin signed rank test for paired samples unless otherwise noted, due to their unknown distribution. Unless otherwise indicated, error bars represent SEM. Statistical analysis were done using MATLAB (Mathworks). In this paper, statistical significance levels are depicted as * for $p < 0.05$, ** for $p < 0.01$, or *** for $p < 0.001$.

## DATA AND SOFTWARE AVAILABILITY

SLM control code is available at https://github.com/wjyangGithub/Volumetric-Imaging. Raw imaging datasets are available upon request.

## Supplementary Material

Refer to Web version on PubMed Central for supplementary material.

## REFERENCES

Alivisatos AP, Chun M, Church GM, Greenspan RJ, Roukes ML, and Yuste R (2012). The brain activity map project and the challenge of functional connectomics. Neuron 74, 970–974. [PubMed: 22726828]

Attinger A, Wang B, and Keller GB (2017). Visuomotor coupling shapes the functional development of mouse visual cortex. Cell 169, 1291–1302.e14. [PubMed: 28602353]

Avitan L, Pujic Z, Mölter J, Van De Poll M, Sun B, Teng H, Amor R, Scott EK, and Goodhill GJ (2017). Spontaneous activity in the zebrafish tectum reorganizes over development and is influenced by visual experience. Curr. Biol 27, 2407–2419.e4. [PubMed: 28781054]

Blondel VD, Guillaume J-L, Lambiotte R, and Lefebvre E (2008). Fast unfolding of communities in large networks. J. Stat. Mech. Theory Exp 2008, P10008.

Bonhoeffer T, and Grinvald A (1991). Iso-orientation domains in cat visual cortex are arranged in pinwheel-like patterns. Nature 353, 429–431. [PubMed: 1896085]

Botcherby EJ, Juškaitis R, Booth MJ, and Wilson T (2008). An optical technique for remote focusing in microscopy. Opt. Commun 281, 880–887.

Botcherby EJ, Smith CW, Kohl MM, Débarre D, Booth MJ, Juškaitis R, Paulsen O, and Wilson T (2012). Aberration-free three-dimensional multiphoton imaging of neuronal activity at kHz rates. Proc. Natl. Acad. Sci. U S A 109,2919–2924. [PubMed: 22315405]

Buchanan EK, Kinsella I, Zhou D, Zhu R, Zhou P, Gerhard F, Ferrante J, Ma Y, Kim S, Shaik M, et al. (2018). Penalized matrix decomposition for denoising, compression, and improved demixing of functional imaging data. bioRxiv. 10.1101/334706.

Carandini M (2004). Amplification of trial-to-trial response variability by neurons in visual cortex. PLoS Biol. 2, E264. [PubMed: 15328535]

Carrillo-Reid L, Miller JE, Hamm JP, Jackson J, and Yuste R (2015). Endogenous sequential cortical activity evoked by visual stimuli. J. Neurosci 35, 8813–8828. [PubMed: 26063915]

Carrillo-Reid L, Yang W, Kang Miller JE, Peterka DS, and Yuste R (2017a). Imaging and optically manipulating neuronal ensembles. Annu. Rev. Biophys 46, 271–293. [PubMed: 28301770]

Carrillo-Reid L, Han S, Taralova E, Jebara T, and Yuste R (2017b). Identification and Targeting of Cortical Ensembles. bioRxiv. 10.1101/226514.

Chen T-W, Wardill TJ, Sun Y, Pulver SR, Renninger SL, Baohan A, Schreiter ER, Kerr RA, Orger MB, Jayaraman V, et al. (2013). Ultrasensitive fluorescent proteins for imaging neuronal activity. Nature 499, 295–300. [PubMed: 23868258]

Cheng A, Gonçalves JT, Golshani P, Arisaka K, and Portera-Cailliau C (2011). Simultaneous two-photon calcium imaging at different depths with spatiotemporal multiplexing. Nat. Methods 8, 139–142. [PubMed: 21217749]

Constantinople CM, and Bruno RM (2013). Deep cortical layers are activated directly by thalamus. Science 340, 1591–1594. [PubMed: 23812718]

Cossart R, Aronov D, and Yuste R (2003). Attractor dynamics of network UP states in the neocortex. Nature 423, 283–288. [PubMed: 12748641]

Dana H, Mohar B, Sun Y, Narayan S, Gordus A, Hasseman JP, Tsegaye G, Holt GT, Hu A, Walpita D, et al. (2016). Sensitive red protein calcium indicators for imaging neural activity. eLife 5, e12727. [PubMed: 27011354]

Denk W, Strickler J, and Webb W (1990). Two-photon laser scanning fluorescence microscopy. Science 248, 73–76. [PubMed: 2321027]

Douglas RJ, and Martin KAC (2004). Neuronal circuits of the neocortex. Annu. Rev. Neurosci 27, 419–451. [PubMed: 15217339]

Dubbs A, Guevara J, and Yuste R (2015). Moco: Fast Motion Correction for Calcium Imaging. Front. Neuroinform 10, 6.

Duemani Reddy G, Kelleher K, Fink R, and Saggau P (2008). Three-dimensional random access multiphoton microscopy for functional imaging of neuronal activity. Nat. Neurosci 11, 713–720. [PubMed: 18432198]

Frey BJ, and Dueck D (2007). Clustering by passing messages between data points. Science 315, 972–976. [PubMed: 17218491]

Gilbert CD, and Sigman M (2007). Brain states: top-down influences in sensory processing. Neuron 54, 677–696. [PubMed: 17553419]

Göbel W, and Helmchen F (2007). New angles on neuronal dendrites in vivo. J. Neurophysiol. 98, 3770–3779. [PubMed: 17898141]

Grewe BF, Voigt FF, van't Hoff M, and Helmchen F (2011). Fast two-layer two-photon imaging of neuronal cell populations using an electrically tunable lens. Biomed. Opt. Express 2, 2035–2046. [PubMed: 21750778]

Helmchen F, and Denk W (2005). Deep tissue two-photon microscopy. Nat. Methods 2, 932–940. [PubMed: 16299478]

Hubel DH, and Wiesel TN (1962). Receptive fields, binocular interaction and functional architecture in the cat'svisual cortex. J. Physiol 160,106–154. [PubMed: 14449617]

Inoue M, Takeuchi A, Horigane S, Ohkura M, Gengyo-Ando K, Fujii H, Kamijo S, Takemoto-Kimura S, Kano M, Nakai J, et al. (2015). Rational design of a high-affinity, fast, red calcium indicator R-CaMP2. Nat. Methods 12, 64–70. [PubMed: 25419959]

Ji N, Sato TR, and Betzig E (2012). Characterization and adaptive optical correlation of aberrations during *in vivo* imaging in the mouse cortex. Proc. Natl. Acad. Sci 109, 22–27. [PubMed: 22190489]

Ji N, Freeman J, and Smith SL (2016). Technologies for imaging neural activity in large volumes. Nat. Neurosci 19, 1154–1164. [PubMed: 27571194]

Katona G, Szalay G, Maák P, Kaszás A, Veress M, Hillier D, Chiovini B, Vizi ES, Roska B, and Rózsa B (2012). Fast two-photon in vivo imaging with three-dimensional random-access scanning in large tissue volumes. Nat. Methods 9, 201–208. [PubMed: 22231641]

Kerlin A, Mohar B, Flickinger D, MacLennan BJ, Davis C, Spruston N, and Svoboda K (2018). Functional clustering of dendritic activity during decision-making. bioRxiv. 10.1101/440396.

Kiani R, Cueva CJ, Reppas JB, Peixoto D, Ryu SI, and Newsome WT (2015). Natural grouping of neural responses reveals spatially segregated clusters in prearcuate cortex. Neuron 85, 1359–1373. [PubMed: 25728571]

Kisley MA, and Gerstein GL (1999). Trial-to-trial variability and state-dependent modulation of auditory-evoked responses in cortex. J. Neurosci 19, 10451–10460. [PubMed: 10575042]

Lancichinetti A, and Fortunato S (2012). Consensus clustering in complex networks. Sci. Rep 2, 336. [PubMed: 22468223]

Li Y, Lu H, Cheng PL, Ge S, Xu H, Shi S-H, and Dan Y (2012). Clonally related visual cortical neurons show similar stimulus feature selectivity. Nature 486, 118–121. [PubMed: 22678292]

Lopes-dos-Santos V, Ribeiro S, and Tort ABL (2013). Detecting cell assemblies in large neuronal populations. J. Neurosci. Methods 220, 149–166. [PubMed: 23639919]

Love GD (1997). Wave-front correction and production of Zernike modes with a liquid-crystal spatial light modulator. Appl. Opt 36, 1517–1520. [PubMed: 18250829]

Luczak A, Barthó P, Marguet SL, Buzsáki G, and Harris KD (2007). Sequential structure of neocortical spontaneous activity in vivo. Proc. Natl. Acad. Sci. USA 104, 347–352. [PubMed: 17185420]

Mao BQ, Hamzei-Sichani F, Aronov D, Froemke RC, and Yuste R (2001). Dynamics of spontaneous activity in neocortical slices. Neuron 32, 883–898. [PubMed: 11738033]

Miller JE, Ayzenshtat I, Carrillo-Reid L, and Yuste R (2014). Visual stimuli recruit intrinsically generated cortical ensembles. Proc. Natl. Acad. Sci. USA 111, E4053–E4061. [PubMed: 25201983]

Niell CM, and Stryker MP (2008). Highly selective receptive fields in mouse visual cortex. J. Neurosci 28, 7520–7536. [PubMed: 18650330]

Niell CM, and Stryker MP (2010). Modulation of visual responses by behavioral state in mouse visual cortex. Neuron 65, 472–479. [PubMed: 20188652]

Ohki K, and Reid RC (2007). Specificity and randomness in the visual cortex. Curr. Opin. Neurobiol 17, 401–407. [PubMed: 17720489]

Ohki K, Chung S, Ch'ng YH, Kara P, and Reid RC (2005). Functional imaging with cellular resolution reveals precise micro-architecture in visual cortex. Nature 433, 597–603. [PubMed: 15660108]

Peron SP, Freeman J, Iyer V, Guo C, and Svoboda K (2015). A cellular resolution map of barrel cortex activity during tactile behavior. Neuron 86, 783–799. [PubMed: 25913859]

Pnevmatikakis EA, Soudry D, Gao Y, Machado TA, Merel J, Pfau D, Reardon T, Mu Y, Lacefield C, Yang W, et al. (2016). Simultaneous denoising, deconvolution, and demixing of calcium imaging data. Neuron 89, 285–299. [PubMed: 26774160]

Pologruto TA, Sabatini BL, and Svoboda K (2003). ScanImage: Flexible software for operating laser scanning microscopes. Biomed. Eng. Online 2,13. [PubMed: 12801419]

Ringach DL, Mineault PJ, Tring E, Olivas ND, Garcia-Junco-Clemente P, and Trachtenberg JT (2016). Spatial clustering of tuning in mouse primary visual cortex. Nat. Commun 7, 12270. [PubMed: 27481398]

Rochefort NL, Narushima M, Grienberger C, Marandi N, Hill DN, and Konnerth A (2011). Development of direction selectivity in mouse cortical neurons. Neuron 71, 425–432. [PubMed: 21835340]

Rubinov M, and Sporns O (2010). Complex network measures of brain connectivity: uses and interpretations. Neuroimage 52, 1059–1069. [PubMed: 19819337]

Rupprecht P, Prendergast A, Wyart C, and Friedrich RW (2016). Remote z-scanning with a macroscopic voice coil motor for fast 3D multiphoton laser scanning microscopy. Biomed. Opt. Express 7, 1656–1671. [PubMed: 27231612]

Smith MA, and Kohn A (2008). Spatial and temporal scales of neuronal correlation in primary visual cortex. J. Neurosci 28, 12591–12603. [PubMed: 19036953]

Stirman JN, Smith IT, Kudenov MW, and Smith SL (2016). Wide field-of-view, multi-region, two-photon imaging of neuronal activity in the mammalian brain. Nat. Biotechnol 34, 857–862. [PubMed: 27347754]

Tian L, Hires SA, Mao T, Huber D, Chiappe ME, Chalasani SH, Petreanu L, Akerboom J, McKinney SA, Schreiter ER, et al. (2009). Imaging neural activity in worms, flies and mice with improved GCaMP calcium indicators. Nat. Methods 6, 875–881. [PubMed: 19898485]

Tzvetanov T (2016). Commentary: Robust quantification of orientation selectivity and direction selectivity. Front. Neural Circuits 10, 92. [PubMed: 27932956]

Yang W (2018). Volumetric-Imaging. GitHub. https://github.com/wjyangGithub/Volumetric-Imaging.

Yang W, and Yuste R (2017). In vivo imaging of neural activity. Nat. Methods 14, 349–359. [PubMed: 28362436]

Yang W, Miller JE, Carrillo-Reid L, Pnevmatikakis E, Paninski L, Yuste R, and Peterka DS (2016). Simultaneous multi-plane imaging of neural circuits. Neuron 89, 269–284. [PubMed: 26774159]

Yuste R (2015). From the neuron doctrine to neural networks. Nat. Rev. Neurosci. 16, 487–497. [PubMed: 26152865]

Yuste R, and Denk W (1995). Dendritic spines as basic functional units of neuronal integration. Nature 375, 682–684. [PubMed: 7791901]

Yuste R, and Katz LC (1991). Control of postsynaptic Ca2+ influx in developing neocortex by excitatory and inhibitory neurotransmitters. Neuron 6, 333–344. [PubMed: 1672071]

## Highlights

- Fast volumetric imaging of cortical columns *in vivo* with hybrid wavelength multiplexing

- Functional correlations across cortical layers vary from trial to trial

- Lack of columnar structures in orientation responses in mouse V1

- Simultaneous imaging of axonal projections and neuronal populations in 3D
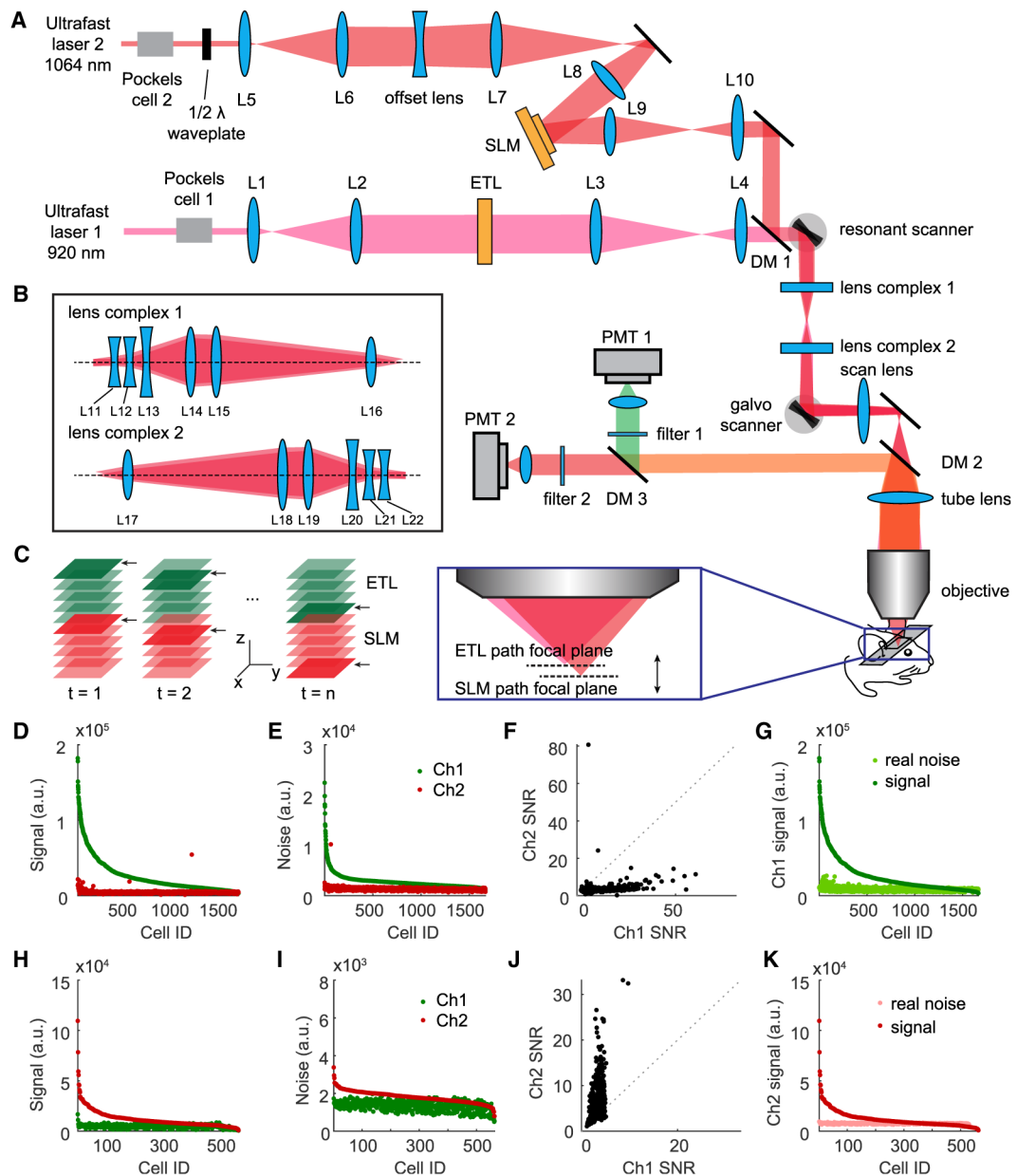
**Figure 1. Two-Color Two-Photon Volumetric Imaging Microscope**

(A) Microscope design diagram. Two lasers at 920 and 1,064 nm are expanded in beam spatial profile and modulated by an ETL unit and an SLM unit, correspondingly, then combined through a dichroic mirror and passed through a resonant scanner and a galvanometric scanner before exciting the sample through an objective lens. Emitted fluorescence is collected through two separate PMTs. The SLM path is also equipped with an offset lens that separates its focal plane (200 μm deeper) from that of the ETL path. See Table S1 for detailed parameters of the optical elements.

(B) Details of the lens complex design.

(C) Diagram of volumetric imaging. Two planes are excited and recorded at the same time: the shallower one from the ETL path and the deeper one from the SLM path. The imaging depth of the dual planes cycles over time to record a three-dimensional (3D) volume.

(D–F) Measured signal (D), noise (E), and signal-to-noise ratio (SNR) (F) from both green (Ch1) and red (Ch2) PMTs, with only 920 nm laser on.

(G) Quantified signal strength with effective noise in green channel (Ch1). Signal strength is from signal in (D) (green dots). Effective noise is computed as the sum of noise in (E), signal in (H), and noise in (I) (all in green dots).

(H–J) Measured signal (H), noise (I), and SNR (J) from both green (Ch1) and red (Ch2) PMTs, with only 1,064 nm laser on.

(K) Quantified signal strength with effective noise in red channel (Ch2). Signal strength is from signal in (H) (red dots). Effective noise is computed as the sum of noise in (I), signal in (D), and noise in (E) (all in red dots). n = 3 experiments.

See also Figures S1-S3 and Table S1.
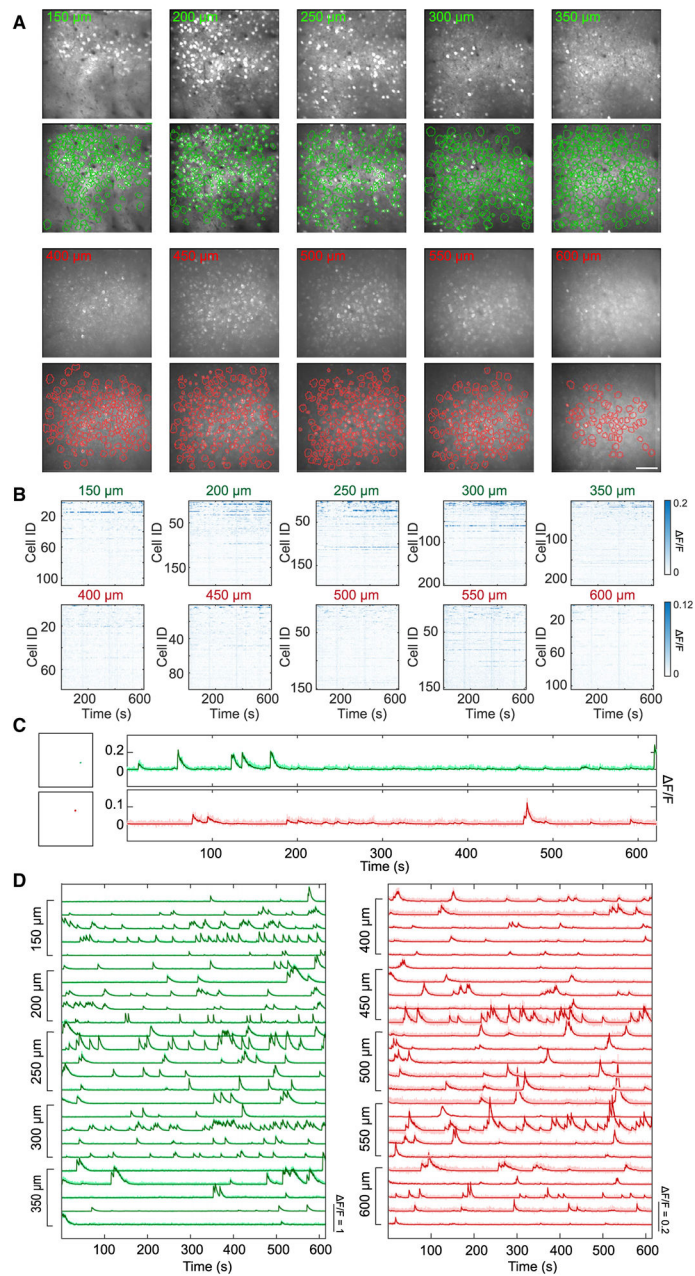
**Figure 2. *In Vivo* Volumetric Imaging of Cortical Columns**

(A) Row 1, temporal average images of recorded planes in Ch1 with 920 nm laser, recorded from 150 to 350 μm, with a spacing of 50 μm. Row 2, ROI contours extracted by the CNMF algorithm, overlaid with temporal average images. Row 3, temporal average images of recorded planes in Ch2 with 1,064 nm laser, recorded from 400 to 600 μm, with a spacing of 50 μm. Row 4, ROI contours extracted by the CNMF algorithm, overlaid with temporal average images. Scale bar: 100 μm.

(B) Raw ΔF/F traces from all extracted ROIs in each plane, over 10 min spontaneous activity.

(C) Two examples of raw (light color) and deconvolved (dark color) traces, from 920 and 1,064 nm path.
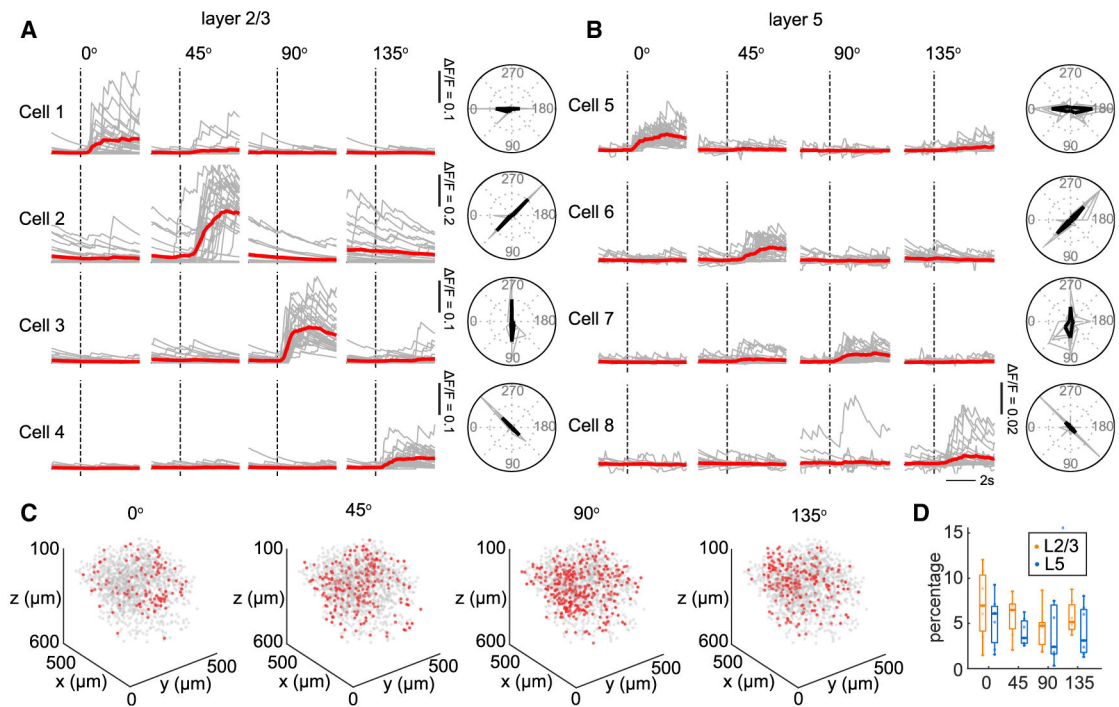
(D) Example traces from each plane. Light color, raw traces. Dark color, deconvolved traces. See also Figure S4 and Video S1.

**Figure 3. Orientation-Tuning Cells in V1 Columns**

(A and B) Fluorescence traces (left) and polar graphs (right) of representative cells that are selective to 0°, 45°, 90°, and 135° drifting gratings in layer 2/3 (A) and layer 5 (B).

(C) 3D distribution of orientation-selective cells in the imaged cortical column from a representative dataset.

(D) Percentage of orientation-selective cells in layer 2/3 and layer 5 (n = 7 experiments).
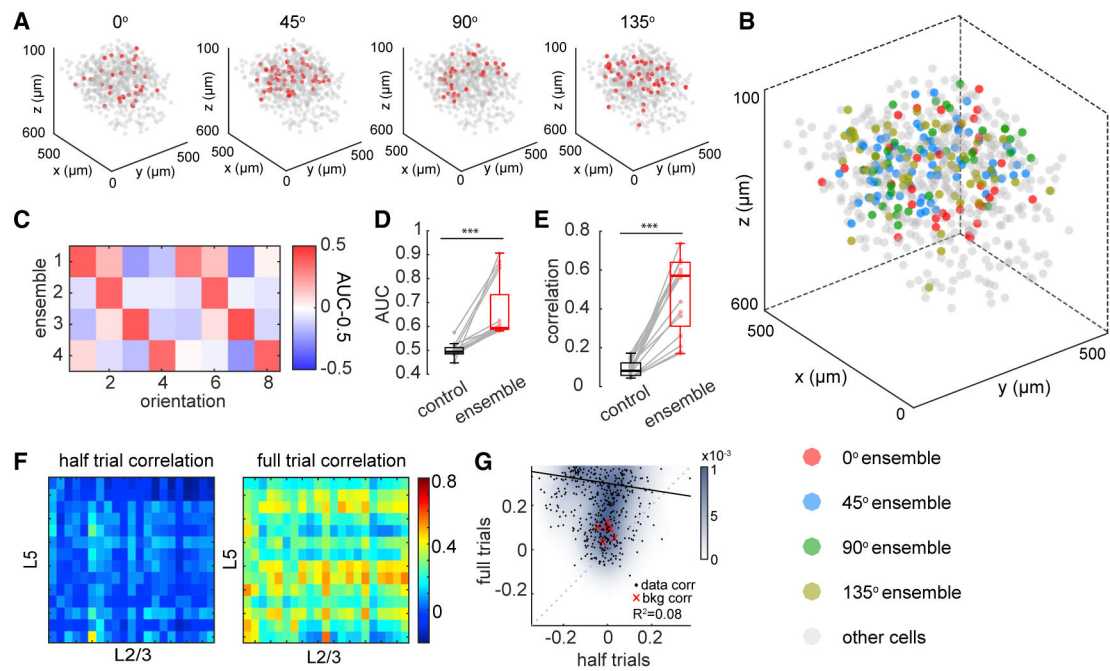
**Figure 4. Correlation Structure of Visually Evoked Ensembles**

(A) Example of 3D structures of visually evoked ensembles in the imaged cortical column identified with Louvain method and consensus clustering.

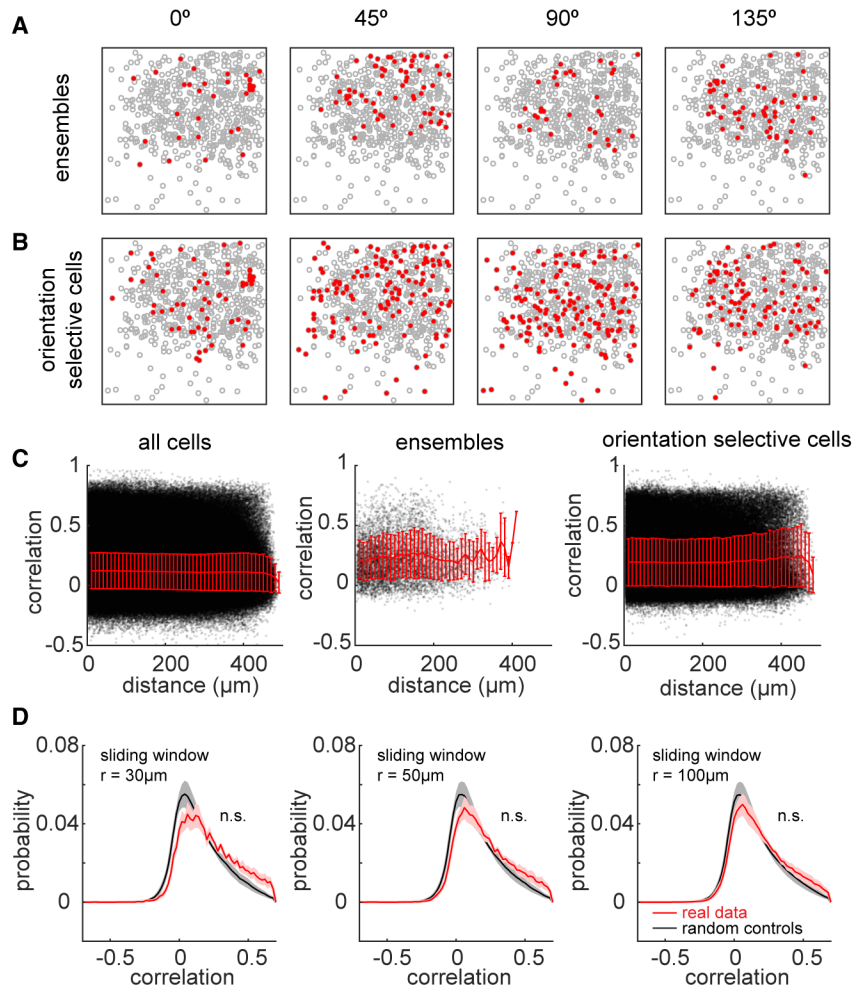(B) 3D view of all visually evoked ensembles, from the same ensembles as (A).

(C) Prediction performance of the ensembles in (A), of all directions. Color represents AUC-0.5; red color represents high prediction performance.

(D) Statistics of ensemble prediction performance, compared with random controls (p < 0.001). Note that the y axis represents AUC; 0.5 on the AUC axis represents chance level.

(E) Statistics of average correlation within ensembles, compared with random controls (p < 0.001). Random controls were generated by random sample subsets of the population with the same number of neurons in corresponding ensembles, for 10 times each ensemble.

(F) Example correlation structure between ensemble cells in layer 2/3 and layer 5, using the first and second half of visual stimulus trials (left) and using the entire trials (right).

(G) Scatterplot of pairwise correlation between layer 2/3 and layer 5 ensemble cells from half trials and full trials. Dashed line represents x = y; black dots represent data point correlations; red crosses represent background correlation from Ch1 and Ch2 in all experiments; black line represents the least squares linear regression result. n = 7 experiments, 16 ensembles.

**Figure 5. Lack of Columnar Structures in V1 Responses**

(A) Example of the spatial locations of visually evoked ensembles (top-projection views from all planes).

(B) Example of spatial locations of orientation-selective cells (top-projection views from all planes). Note the salt-and-pepper structure in both cases.

(C) Scatterplot of pairwise lateral distance and correlation, among all cell pairs (left), among visually evoked ensembles (middle), and among orientation-selective cells (right). Red line shows mean ± SD. Data pooled from six experiments.

(D) Distribution of pairwise correlation within columns of 30, 50, and 100 μm diameter. Red, real data; black, random controls. Random controls were generated by computing the correlation between cells within the column and a random set of cells with the same number outside of the column, repeated 50 times each column. n.s., not significant. Statistical analysis was done using the Wilcoxon rank-sum test in each correlation bin of individual datasets, comparing real data with random controls. All correlation bins above −0.3 were not significant, for all experiments. n = 6 experiments.

See also Figure S5.
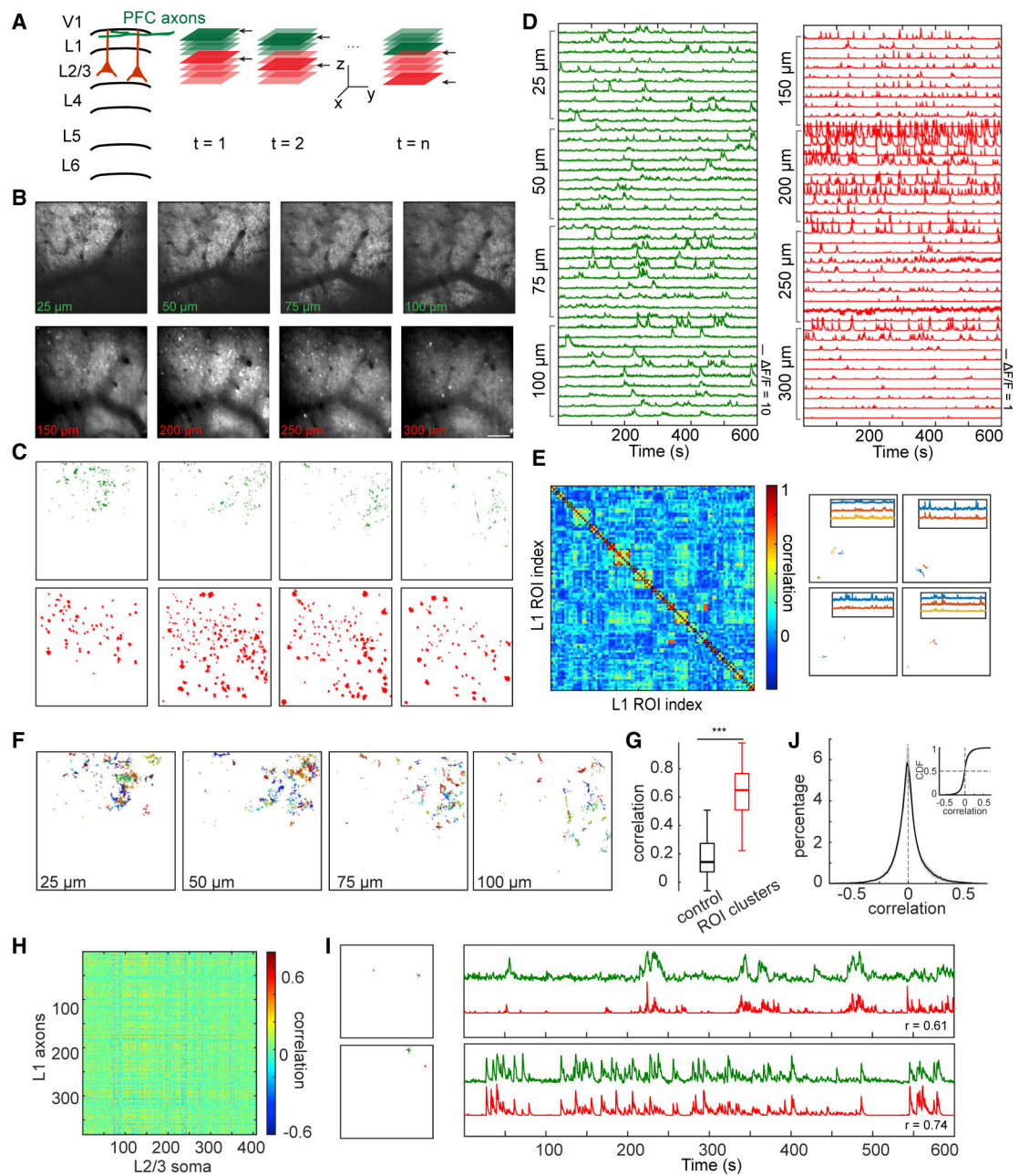
**Figure 6. Volumetric Imaging of Layer 1 Long-Range Axonal Projections from PFC and Local Layer 2/3 Somata in V1**

(A) Schematic of experiment design. In this experiment, the 920 nm laser path covers four planes in layer 1, and the 1,064 nm path covers four planes in layer 2/3.

(B) Examples of average images from the recorded planes, from 25 to 100 μm with a spacing of 25 μm in layer 1 and from 150 to 300 μm with a spacing of 50 μm in layer 2/3. Scale bar: 100 μm.

(C) Examples of extracted ROIs in each plane.

(D) Example traces from each plane.

(E) Example of clustered correlation matrix of all ROIs in layer 1, sorted by cluster identity (left), and four examples of ROIs that are identified in the same clusters with corresponding traces (right). Note that the imaging depth of the example ROIs on the right might be different.

(F) Clustering result in each plane. ROIs belonging to the same cluster are shown with the same color.

(G) Correlation within clusters, compared with random controls ($p < 0.001$, Wilcoxon signed rank test).

(H) Correlation between layer 1 ROIs and layer 2/3 ROIs in one representative dataset.

(I) Two examples of ROI pairs from layer 1 (green) and layer 2/3 (red) that are highly correlated. The lateral locations of ROI pairs are shown on the left, and their traces shown on the right.

(J) Distribution of correlation between layer 1 and layer 2/3 ROIs (individual dataset plotted in gray with their mean plotted in black). Upper right curve shows the cumulative distribution function. $n = 11$ experiments; mean correlation $0.006 \pm 0.012$ ($p = 0.617$, t test). See also Figure S6.

KEY RESOURCES TABLE

| REAGENT or RESOURCE | SOURCE | IDENTIFIER |
|---|---|---|
| Bacterial and Virus Strains | | |
| AAV1.Syn.NES-jRGECO1b.WPRE.SV40 | Dana et al., 2016 | UPenn Vector Core; Addgene 100857-AAV1 |
| AAV9.hSyn.GCaMP6s.WPRE.SV40 | Chen et al., 2013 | UPenn Vector Core; Addgene 100843-AAV9 |
| Experimental Models: Organisms/Strains | | |
| Mouse (wild-type, C57BL/6J) | Jackson Laboratory | N/A |
| Software and Algorithms | | |
| ImageJ | NIH | https://imagej.nih.gov/ij/ |
| Moco | Dubbs et al., 2015 | https://github.com/NTCColumbia/moco |
| MATLAB(R2016a) | MathWorks | https://www.mathworks.com/ |
| SLM control software | This paper | https://github.com/wjyangGithub/Volumetric-Imaging |
| Constrained nonnegative matrix factorization (CNMF) algorithm | Pnevmatikakis et al., 2016 | https://github.com/flatironinstitute/CaImAn-MATLAB |
| Penalized matrix decomposition (PMD) algorithm | Buchanan et al., 2018 | https://github.com/paninski-lab/funimag |